




Numerical calibration method for a multiple spectrometer-based OCT system

YUSI MIAO,¹  JUN SONG,² DESTINY HSU,³ RINGO NG,³ YIFAN JIAN,⁴ MARINKO V. SARUNIC,^{3,5,6} AND MYEONG JIN JU^{1,2,*}

¹Department of Ophthalmology and Visual Sciences, University of British Columbia, Vancouver, BC, Canada

²School of Biomedical Engineering, University of British Columbia, Vancouver, BC, Canada

³School of Engineering Science, Simon Fraser University, Burnaby, BC, Canada

⁴Casey Eye Institute, Oregon Health and Science University, Portland, Oregon 97239, USA

⁵Institute of Ophthalmology, University College London, London, UK

⁶Department of Medical Physics and Biomedical Engineering, University College London, London, UK

*myeongjin.ju@ubc.ca

Abstract: The present paper introduces a numerical calibration method for the easy and practical implementation of multiple spectrometer-based spectral-domain optical coherence tomography (SD-OCT) systems. To address the limitations of the traditional hardware-based spectrometer alignment across more than one spectrometer, we applied a numerical spectral calibration algorithm where the pixels corresponding to the same wavelength in each unit are identified through spatial- and frequency-domain interferometric signatures of a mirror sample. The utility of dual spectrometer-based SD-OCT imaging is demonstrated through *in vivo* retinal imaging at two different operation modes with high-speed and dual balanced acquisitions, respectively, in which the spectral alignment is critical to achieve improved retinal image data without any artifacts caused by misalignment of the spectrometers.

© 2022 Optica Publishing Group under the terms of the [Optica Open Access Publishing Agreement](#)

1. Introduction

Fourier-domain optical coherence tomography (FD-OCT) has proven to be an invaluable asset in various applications. Two implementations of FD-OCT, often referred to as spectral-domain (SD) OCT and swept-source (SS) OCT, have both seen wide deployment in ophthalmology, due to their high-sensitivity and non-invasive 3D imaging capability. An important advantage of FD technologies over time-domain (TD) systems is the acquisition speed, as the increased speed allows for wider imaging areas, finer sampling densities, and a reduction of motion artifacts, allowing for improved data analysis during the diagnosis and study of retinal disorders [1–4]. Although both SS-OCT and SD-OCT are implemented in the clinical ophthalmic imaging of both the anterior and posterior segment, it is widely accepted that SD systems generally provide higher spatial resolution due to the shorter operating wavelength, with central wavelengths typically around 800 nm, compared to 1060 nm in SS-OCT [5]. Additionally, SD-OCT allows for exceptional phase stability, owing to simultaneous acquisition of all spectral sampling points via a line-scan camera [2].

The principal factor restricting the imaging speed for SD-OCT is the line-scan camera in the spectrometer, as the A-scan rate of the sensors in the camera limits the maximum performance of the system. While scanning speeds of SS-OCT mainly rely on laser sweep rates, which have been greatly improved over the last decade, most line-scan cameras employed in SD-OCT operate at maximum speeds of 250 kHz, with only the state-of-the-art line-scan cameras with high full well capacity reaching up to 600 kHz [6]. Despite this constraint, several approaches exist to overcome the speed limitations of SD-OCT, with one simple and practical solution being the implementation of multiple spectrometers for detection. Dual spectrometer configurations have

been reported to attain 500 kHz A-scan rates at 850 nm, using a beam splitter to divide the light at the detection arm [7]. Extending from studies on dual spectrometer setups, a 1 MHz A-scan acquisition rate was achieved through the use of four detection spectrometers and a 1×4 optical switch assembly [8]. In addition to the increased acquisition speed, several studies have shown clear advantages in signal-to-noise ratio (SNR) and common noise suppression by applying a dual balanced detection (DBD) technique with two spectrometers [9–12]. Furthermore, a dual spectrometer configuration can be equipped with a polarizing beam splitter, allowing for the detection of polarization-sensitive contrast with a single circular polarization input [13,14].

Despite the increased performance and clinical utility provided by the dual spectrometer-based SD-OCT technologies, they have remained neither readily accessible to research groups nor widely implemented in clinical environments. Aside from the cost of implementing additional spectrometers, this is owing to the difficulties in aligning multiple spectrometers and ensuring comparable performance in each of them. Precise alignment of multiple spectrometers is generally difficult to achieve without external calibration instruments, such as a tunable laser [15] and a calibration lamp [16], which adds additional complexity and increases total cost of the system. Such hardware alignment of multiple spectrometers is also a time-consuming process, as minor misalignments lead to significant degradation of data quality, ultimately rendering multi-spectrometer SD-OCT systems less appealing to clinical practice, in spite of the enhanced performance [17]. A computational approach to correct for the variation in the spectrometer configuration can be more practical, but the previously reported methods are mostly focused on the amplitude correction [9,18] with only a few studies that have attempted to align the wavenumber itself [11,13,19,20]. Nevertheless, the effect of spectral misalignment and the quantitative evaluation of numerical correction in the high-speed SD-OCT and dual balanced detection SD-OCT system has not been extensively studied.

In this manuscript, we address these practical considerations for dual spectrometer SD-OCT design and demonstrate a novel numerical method for calibrating the two spectrometers. This approach corrects spectral misalignment between the spectrometers by applying spatial remapping in the wavelength domain. The proposed method provides a software-based, hardware-agnostic solution for spectral calibration, as it requires no knowledge regarding exact wavenumber in each device, while providing improved performance compared to hardware-only alignment of the optical components in the spectrometers. We will demonstrate these capabilities using calibration data from a mirror, followed by *in vivo* retinal imaging comparisons, showing improved spatial and temporal contrast. Finally, the utility of multiple spectrometer-based SD-OCT in the clinical imaging will be explored.

2. Method

2.1. Dual-spectrometer spectral-domain retinal OCT system

Figure 1 shows the system overview of the dual-spectrometer SD-OCT setup. A broadband superluminescent diode (SLD, BLM2-D-810-B-5, Superlum) with a center wavelength of 810 nm and full width at half maximum of 100 nm is used as the light source. A wideband fiber coupler directs 25% of light from the source into the ophthalmic scanner head, and 75% of the signal from source is directed to the reference path. Then, the returning light from both paths are combined at the 50/50 coupler, from which the two output ports are connected to a separate spectrometer, producing a π shift in phase for balanced detection [10]. Three polarization controllers adjust polarization of the light source, sample arm, and one of the spectrometers of the dual-spectrometer SD-OCT system. The ophthalmic scanner in the sample arm is configured to be identical to our previous study [21], consisting of 2-axis galvanometer and a simple lens relay. The beam diameter and the illumination power incident at the cornea is set to be 1.7 mm ($1/e^2$) and 0.75 mW, respectively. It is worth noting that a 75/25 coupler is used in this study due to the relatively low source output power of the 810 nm SLD (5mW). However, further improvement in the signal

sensitivity and noise suppression may be achieved with a different dual-spectrometer system configuration as recently demonstrated in the balanced-detection visible-light OCT [11,22].

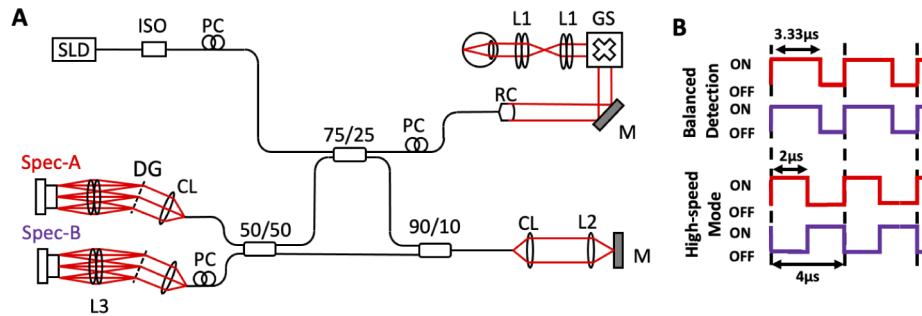


Fig. 1. System configuration of dual-spectrometer retinal SD-OCT system (A) and the camera trigger signals for different operation modes (B). In balanced detection mode, the trigger signals for spectrometer-A (red) and spectrometer-B (blue) are in sync at 250 kHz line-scan rate. In high-speed mode, the trigger signals are π shifted in phase with one another, achieving effective line-scan rate of 500 kHz. Key: CL, collimator; DG, diffraction grating; GS, galvanometer scanner; ISO, optical isolator; L, lens; M, mirror; PC, polarization controller; RC, reflective collimator; Spec, Spectrometer.

The SD-OCT system has two interchangeable operation modes, high-speed mode and dual-balanced detection mode, controlled by a simple inverter logic gate circuit connected to the line-scan cameras (Octoplus, Teledyne e2v Ltd, UK) of each spectrometer. Data from the two line-scan cameras are sent to a data acquisition computer via a frame grabber (PCIe-1437, National Instruments, TX, USA) and two camera link cables. In both modes, each of the spectrometer is operating at the maximum speed of the line-scan camera at 250 kHz, which is equivalent to the line period of 4.0 μs. During high-speed mode, the camera operation trigger passes through the logic gate and is imposed alternately to each spectrometer, allowing one detector to operate while the other is down with an exposure time of 2.0 μs. In this operation mode, the system could acquire data at a 100% duty cycle without any integration of dead time, achieving effectively 500 kHz A-scan rate, twice as fast compared to the maximum speed of a single line-scan camera. During dual-balanced detection mode, the camera operation trigger bypasses the logic gate circuit and the two detectors receive a synchronized trigger with an exposure time of 3.3 μs. When operating in balanced detection mode, the balanced detectors receive interference signals simultaneously, but with one a π shifted in phase, for acquiring OCT images with higher SNR.

2.2. Hardware alignment of the custom-designed spectrometer

The optical components of the custom-built spectrometer are designed using Zemax OpticStudio (Zemax, LLC, WA, USA) and placed into an aluminum plate enclosure. The plate, manufactured by high-precision CNC machining, provides rough alignment of the optical component with a tolerance of 0.01 mm for every cut, equivalent to the potential deviation caused by the machine. The fine alignment of the spectrometers is performed by adjusting the flexure and kinematic mounts holding the optical components, while tracking the signal with real-time monitoring software to match the performance of the two spectrometers.

Figure 2(A) shows the three main optical components from each spectrometer designed with freedom for mechanical adjustment to fine-tune the spectral alignment: turning mirror, diffraction grating and line-scan CMOS camera. The position of the turning mirror determines the path and incident angle of the collimated beam into the grating from the lens collimator. The location and rotation position of the grating adjust the path of diffracted beam into the line-scan camera

passing through the focusing lens. The yaw of line-scan camera used for the spectrometer is adjusted to calibrate the incident angle of the diffracted beam into the camera sensor. The precise mechanical alignment provides similar performance between the two spectrometers as shown in Fig. 2(B) and (C). The axial resolution and the 6 dB sensitivity roll-off of both spectrometer-A and -B are measured as 3.2 μm (in air) and 1.5 mm (in air), respectively. However, we found some residual differences between the acquired spectral interference fringe data, where the fast Fourier transformation (FFT) signals of each spectrometer are visualized at different depth positions. Although the spectrometers were built using identical components and design, we found it very challenging to compensate the residual performance differences in the spectral data through mechanical alignment even with real-time feedback.

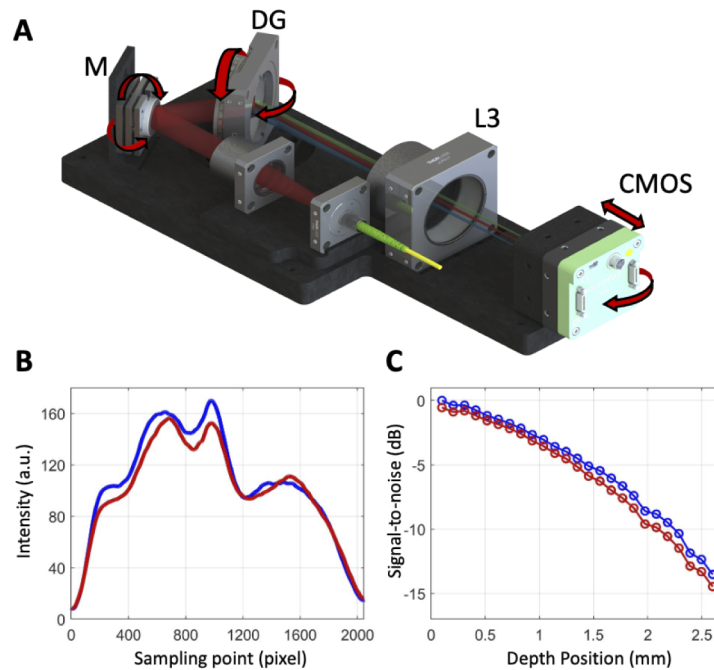


Fig. 2. Schematic of custom-designed spectrometer with degree-of-freedom indicated with red arrows (A). Power spectrum of spectrometer-A and spectrometer-B signals, indicated as red and blue, respectively (B). Sensitivity roll-off of spectrometer-A and spectrometer-B signals, indicated as red and blue, respectively (C). Key: DG, diffraction grating; L, lens; M, mirror.

2.3. Method of numerical spectral alignment

This section presents the concept of numerical spectral alignment in a spectrometer pair. A spectrometer is an optical instrument used to analyze a property of light as a function of its portion of the electromagnetic spectrum, including wavelength, optical frequency, and energy [23]. Typically, this function is mapped onto each unique element of a one-dimensional, or linear, array detector. Hence, an ideal spectrometer pair for the dual spectrometer system will have the identical mapping of the electromagnetic spectrum along linear detector pixels. For example, if the 1st pixel in one spectrometer corresponds to 800 nm wavelength, this must be also true in the paired spectrometer. In practice, this is extremely hard to achieve via mechanical alignment alone, as demonstrated in the previous section. Furthermore, the spectrometer alignment can change over time from the degradation of opto-mechanical components and environmental

conditions. Instead, the proposed method will computationally align the spectrometer pair through interpolation and registration processes based on a set of calibration mirror data. Registration provides a transformation maximizing the similarity measure between the transformed version of spectrometer signal and a second reference spectrometer signal. In the rest of the manuscript, we will refer to the numerical alignment process as *remapping* of spectrometer.

The numerical alignment problem of spectrometer pair can be described as follows: assume the interference signal X is simultaneously recorded from both spectrometers at M optical path length (OPL) positions and N discrete sampling position of the detector (*i.e.*, $X = [x_1, \dots, x_N]$ where $x_n = [x_n[z_1], \dots, x_n[z_M]]$). When the phase of the electrical field in each coupling port is compensated (*e.g.*, π phase shift in the two output ports of 2×2 couplers) and the spectrometer alignment is properly corrected, the interference signals of the two spectrometers at any OPL position should be aligned in phase. The key is to acquire interferometric signals with more than one frequency by adjusting the optical path length differences, as this allows alignment of the interference signals through both spatial- and frequency-domain, adding more constraints to the optimization problem. In the case of one frequency measurement, lack of constraint will often lead to a trivial solution to the alignment problem, leading to the sub-optimum local minima. Therefore, the goal in this problem is to computationally align interference signals recorded from two separate spectrometers to minimize the intensity differences between them at all frequency positions. We calculated the mean square error (MSE) to measure the difference between interference signals, X and Y , at all frequency components,

$$\langle MSE(X, Y') \rangle = \frac{1}{M} \sum_{z=1}^M MSE_z = \frac{1}{MN} \sum_{z=1}^M \sum_{n=1}^N (x_n[z] - y'_n[z])^2, \quad (1)$$

where MSE_z indicates MSE at the OPL position z , $\langle \rangle$ indicates the mean across all M OPL positions. Y' represents the transformed interference signal, the envelop of which is consistent with that of the original signal Y . During the numerical alignment, one of the spectrometer signals is interpolated based on a new set of coordinate points, referred to as *remap look-up table* (LUT). To realize the nonlinear transformation of the spectral signal, the remap LUT are given by adding polynomial terms (a_0, a_1, a_2, a_3) to the initial grid points $l_0 = [1, \dots, N]$:

$$LUT[n] = l_0[n] + a_3 \left(\frac{n}{N}\right)^3 + a_2 \left(\frac{n}{N}\right)^2 + a_1 \left(\frac{n}{N}\right) + a_0, \quad (2)$$

where n is index position. An optimal set of polynomial coefficients $\hat{A} = [\hat{a}_0, \hat{a}_1, \hat{a}_2, \hat{a}_3]$ is estimated by solving optimization problem that minimizes the spectral differences.

$$\hat{A} = \underset{A}{\operatorname{argmin}} \langle MSE(X, Y') \rangle. \quad (3)$$

Here, the constant term (*e.g.*, a_0) and the first order term (*e.g.*, a_1) of polynomial coefficients indicate offset and tilt in spectrometer alignment, respectively. The higher-order terms (*e.g.*, a_2 and a_3) are included to account for other errors in the alignment.

2.4. Algorithm for numerical spectral alignment

The proposed spectral calibration method is composed of three main parts: 1) spectral reshaping, 2) iterative search for optimal polynomial coefficients, and 3) generate remap LUT . The first and second part of the algorithm are illustrated in Fig. 3. The algorithm takes a set of interferometric signals (X, Y) obtained from a flat mirror placed in both the sample and reference arms. Hereafter, we will refer the interference signal X acquired from spectrometer-A as *reference* signal and the interference signal Y acquired from spectrometer-B as *target* signal. To acquire multiple depth positions, signals are recorded simultaneously from the two spectrometers while optical

path length is altered. In this study, we recorded 20 evenly spaced depth positions within the given imaging range to ensure there are enough data points for optimization. For the purpose of alignment, the π phase shift due to the directional coupler is corrected by inverting the signals from one of the spectrometers.

- (1) **Spectral reshaping** : Spectral reshaping process removes DC signal and normalizes the amplitude of the interferograms (X_{Flat} , Y_{Flat}) so that only the fringe pattern is passed down to the next step. First, the DC signal is removed from the spectral interferogram by applying a binary window function to the FFT signals, leaving only the real components corresponding to interference signal. Then, the signals are converted back to the original domain by performing an inverse Fourier transformation. Next, the amplitude of the fringe is normalized by dividing the signal by its own envelop. Removing the amplitude contribution is of the utmost importance in performing reliable optimization in the next step as amplitude is not only dependent on the spectral alignment but also on other factors such as the wavenumber-dependent coupling loss in the fiber coupler [17].
- (2) **Iterative search for optimal remap coefficients** : In this step, the center portion of the reference spectral signal X_{New} is mapped and registered to the target spectral signal Y_{New} to find a matching portion of the two spectrometers. First, the center portion of the reference spectral signal is extracted based on a given boundary condition. In this study, we empirically set the boundary condition as 20 pixels from the beginning and the end of the data based a rough estimation of spectral alignment from the power spectra. This boundary condition is to ensure that the selected portion of the reference data will always fall in the range of the recorded data by the target spectrometer, and, hence, the algorithm will reliably find a matching portion of the spectrum in the target data. In each iteration of the optimization loop, the target spectral signals are interpolated and transformed based on a new remap LUT in Eq. (2). Initial coordinates for the remap LUT are set as the selected coordinate points of the reference signals to ensure the reference and target spectra contain the same data size, namely $l_0 = [21, 22, \dots, 2028]$ in our case. During the optimization, the polynomial coefficients are iteratively updated to minimize the spectral difference $\langle MSE \rangle$, set as the cost function. Our optimization algorithm can be described as coordinate descent method with random restarts. In coordinate descent, local search of an optimum solution is performed by repeatedly minimizing the cost function in one direction along with a set of different directions, each time starting from the minimum found in the previous direction using a 1-D minimization method [24]. For spectral alignment of interference signals, optimization of the translation (a_0) and of the tilt (a_1) are the most important elements in the alignment. Hence, we optimize the parameters in the order (a_0, a_1, a_2, a_3). 1-D minimization of each parameter is performed using bisection method with pre-defined number of steps [25]. To improve the chance of finding a global minimum, initial points of coordinate search are randomly chosen, and the local optimizations are repeated up to a pre-defined maximum of iterations. Then, a locally optimized point with the lowest cost value is picked as the optimum solution. Although a wide range of optimization algorithms can be employed for the numerical spectrometer alignment, our optimization method mainly focuses on alignment accuracy rather than computational time.
- (3) **Generate remap LUT** : After optimization, the remap LUT is generated based on the optimal polynomial coefficients and Eq. (2). Since the new coordinate points need to be within range of the original coordinate (e.g., $1 - 2048$), certain portions of the spectral signal that violate this rule need to be disregarded from both spectrometers. As a result, the spectrometer after remapping will contain fewer data points than the original. In our case, the data size after remapping is reduced to 2037 points. It is important to note that the amount of overlap in the wavelength range will depend on the initial mechanical alignment

of the spectrometer pair, and therefore, better mechanical alignment will lead to more data points after remapping. Different interpolation techniques can be applied to alter the data size of spectral signals; however, aliasing artifacts at higher frequency components can be generated if the sampling frequency is higher than the original data.

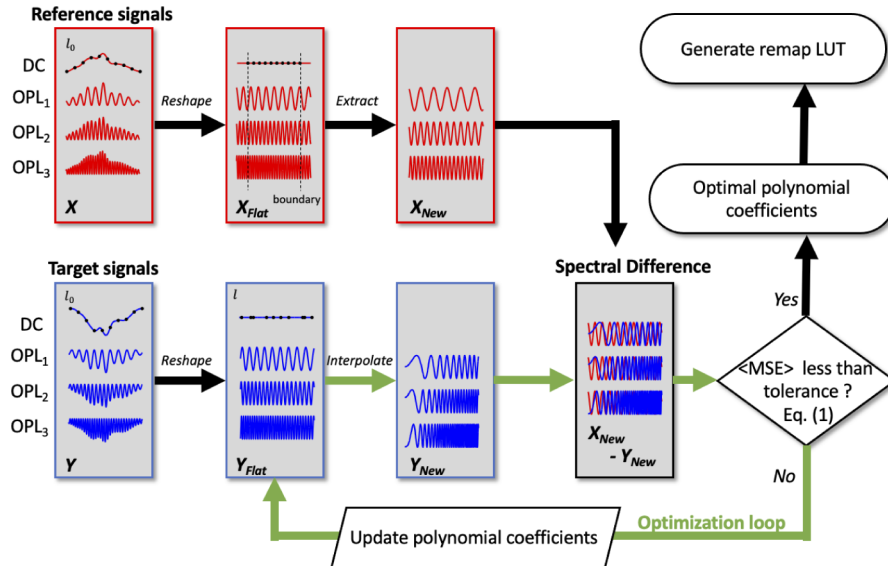


Fig. 3. Signal processing workflow for numerical spectral calibration during spectral reshaping and iterative optimized search steps. X_{Flat} and Y_{Flat} represent the target and reference interferograms after spectral reshaping, respectively. X_{New} and Y_{New} represent the reference and target interferograms after remapping, respectively.

After the numerical spectral alignment, the interferometric component of the spectral data from the two spectrometers can be considered identical. Therefore, we can transform the spectral signal into a linear-in-wavenumber signal using the same wavenumber resampling parameters. There are different methods to linearize wavenumber but we found the phase linearization algorithm [26] works well in our case.

3. Results

3.1. Experimental validation on the calibration mirror

Effects of numerical spectral alignment were first validated using a flat mirror positioned at different depth locations. The obtained signals are analyzed both in the raw fringe form and after FFT. Figure 4 shows the FFT intensity plot of mirror signals before and after numerical calibration. Before the calibration, FFT signals from each spectrometer are shifted with respect to each other, indicating the frequency mismatch in the interferograms. After the numerical alignment process, the peak positions of the FFT signals are well aligned, indicating the spectrometers are properly calibrated. The zoomed-in portion of the last FFT signal shows the signals are aligned at the peak position.

Figure 5 shows representative results from the balanced detection configuration from the two spectrometers before and after numerical calibration. Balanced detection is based on subtraction of the two π -shifted interferograms, and hence the amplitude of the balanced signal is sensitive to the spectral alignment. Here, to make the qualitative assessment of the spectral alignment easier, the signal amplitude of the fringe from each spectrometer is normalized and reshaped

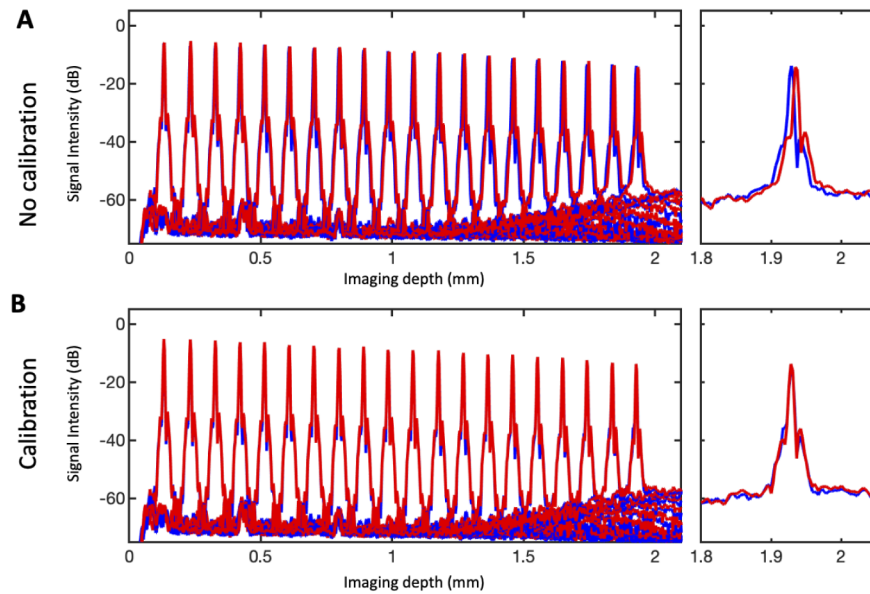


Fig. 4. Depth-dependent intensity plots acquired from a mirror sample. Red indicate FFT signal from spectrometer-A and blue indicate FFT signal from spectrometer-B. The two signals with a corresponding location are well aligned after the numerical calibration.

into a Gaussian distribution. Before calibration, the balanced signals show attenuation at certain fringe frequencies, indicating the similarity of the two spectra is low. After numerical calibration, the amplitude of the balanced fringe signals follows the Gaussian distribution at all frequencies, indicating high degree of alignment in the spectra.

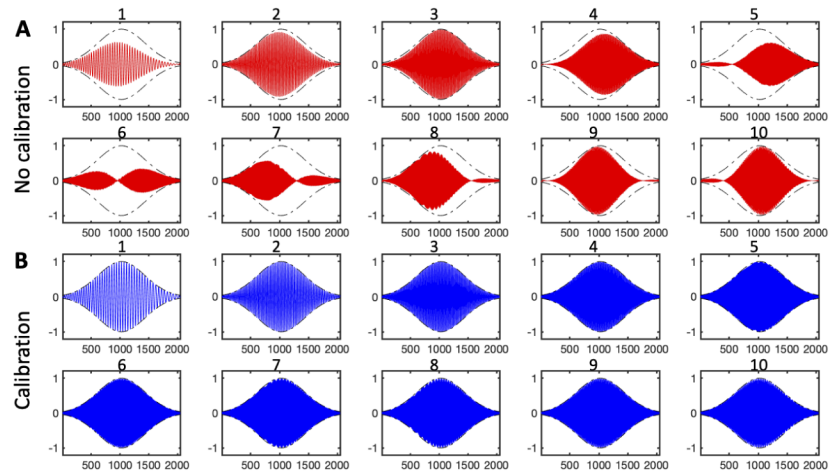


Fig. 5. The amount of fringe alignment as evaluated using spectral subtraction approach, where the normalized spectral signals from each spectrometer are subtracted from one another. The dotted lines indicate the perfectly balanced detection scenario with no signal cancellation between the two fringe signals. The number (*e.g.*, 1-10) above each figure indicates the order of signal from 1 being the low-frequency interferogram taken near DC and 10 being the high-frequency interferogram taken far from DC.

Figure 6 shows quantitative analysis results obtained from testing a mirror as the sample. In Fig. 6(A), cost function is plotted with respect to the changes in the polynomial coefficients in Eq. (2) during one of the optimization loop. Here, cost function is the mean spectral differences between the two spectrometers at all frequency components defined in Eq. (1). After optimization loops, the optimal set of polynomial coefficients were found to be $[\hat{a}_0, \hat{a}_1, \hat{a}_2, \hat{a}_3] = [9.0257, -1.9151, -0.3853, -0.1750]$. Figure 6(B) is the peak positions in the FFT intensity plots shown in Fig. 5, confirming that the shift in the peak position is corrected after numerical alignment. Figure 6(C) is the MSE in Eq. (1) estimated from the amplitude-normalized interferograms from the two spectrometers, indicating the MSE is decreased after optimization. Figure 6(D) shows the peak signal intensity of balanced signals and single spectrometer signals. In an ideal situation where the signals to be balanced are perfectly in anti-phase, the peak of the signal intensity is increased by 6 dB. The result indicates that the sensitivity of the balanced signal is fluctuated and even lower compared to the single detector in some cases without numerical alignment. Therefore, we can conclude that numerical alignment is paramount for proper implementation of balanced detection in a spectrometer-based system.

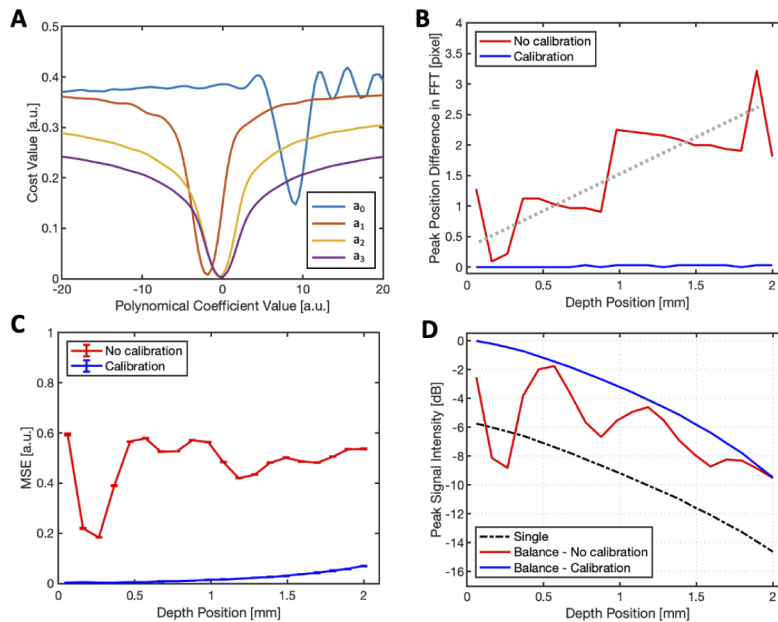


Fig. 6. Quantitative evaluation of the numerical calibration using calibration mirror signals. An example of cost function estimation with respect to the changes in the polynomial coefficient values during an optimization loop (A). The peak positions in the FFT intensity plots are well matched after the spectral calibration (B). The MSE of the normalized spectral intensity in the two spectrometers are significantly reduced after calibration (C). Comparison of peak signal sensitivity between the single spectrometer case, balanced detection of two spectrometers without numerical calibration, and balanced detection of two spectrometers with numerical calibration (D).

3.2. In vivo validation of the numerical spectral alignment: high-speed mode

Figure 7 compares the OCT B-scan images processed with and without the application of numerical calibration at the high-speed mode where the two spectrometers acquire signals alternately at an effective A-scan rate of 500 kHz. Each B-scan is acquired at an effective frame rate of 714 Hz, including 500 A-scans of usable portion and 200 A-scans of flyback. For the sake

of validating the differences in the imaging quality in high-speed scanning mode, the B-scans were further processed by averaging 6 adjacent frames with the B-scan interval of $6\ \mu\text{m}$ to further enhance the contrast. Figure 7(A) and (C) are the *in vivo* retinal images based on the same data acquired while (B) and (D) are the zoomed-in images focusing on the internal limiting membrane (ILM) area of (A) and (C) respectively. For the B-scan image without numerical calibration where spectral misalignment still exists between the spectrometers, noticeable jitter appears at the surface of ILM in the OCT image as demonstrated in Fig. 7(B), and fine features of the images would also be lost after averaging which originate from height mismatch of the A-lines. On the other hand, the B-scan image for which the spectral misalignment was corrected shows a smooth ILM surface without jittering artifacts as illustrated in Fig. 7(D).

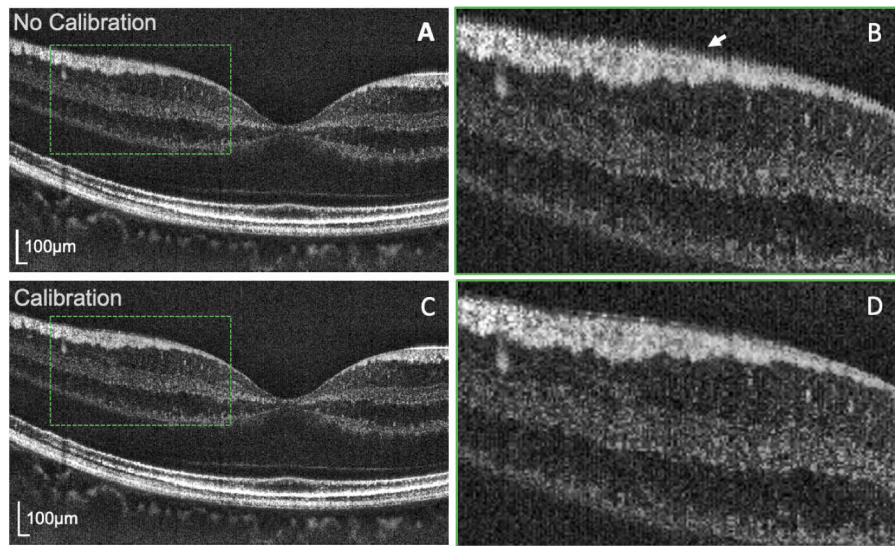


Fig. 7. *In vivo* retinal image with high-speed mode without the numerical spectral calibration (A) and with the numerical spectral calibration (C). The zoom-in images showing the hyper-reflective feature of ILM, indicated by white arrow, is lost without calibration (B) but preserved in the case of images acquired with calibration (D).

In high-speed imaging mode, active optical devices such as optical switches can be implemented to further improve the sensitivity [8]. In principle, optical switches can direct more light to the detector compared to optical couplers, where only part of the light is utilized at the detector. However, implementing optical switches adds additional complexity to the system compared to passive optical devices such as optical couplers. In addition, optical switches will limit the operation mode of the imaging system to only the high-speed mode, as the dual balanced detection mode relies on simultaneous detection of interferometric signals. Our dual spectrometer imaging system is configured to have the flexibility to easily switch between the two imaging modes (*e.g.*, high-speed and balanced detection mode) depending on the application.

3.3. *In vivo* validation of the numerical spectral alignment: balanced detection mode

Figure 8 compares the representative OCT B-scan images processed with and without the application of numerical calibration at the balanced detection mode at an effective A-scan rate of 250 kHz. Each B-scan is acquired at an effective frame rate of 416 Hz, including 500 A-scans of usable portion and 100 A-scans of flyback after the dual-balanced detection. For the sake of validating the improvement in the imaging quality, the B-scans were further processed by averaging 4 adjacent frames with the B-scan interval of $6\ \mu\text{m}$ to enhance the imaging contrast.

Theoretically, the signal power detected from DBD is twice as high compared to the single detector case assuming insertion loss to be negligible if the two spectrometers are perfectly aligned to each other. However, in practice, it is extremely hard to achieve such condition and misalignment between the spectrometers cause signal wash-out that significantly affect the image contrast. Figure 8(A) demonstrates the differences in signal at inner retina (nerve fiber layer, ganglion cell layer, inner plexiform layer, inner nuclear layer, outer plexiform layer) where images processed with numerical calibration method illustrates higher signal based on the A-scan intensity profile. Figure 8(B) demonstrates more noticeable effect of signal wash-out where the choroid is barely visible for the B-scan image processed without numerical calibration while the image processed with numerical calibration clearly presents the choroid. The signal attenuation at the inner retina and choroid can be further confirmed from the A-line intensity profile obtained from the selected locations in the B-scans indicated by the dotted lines.

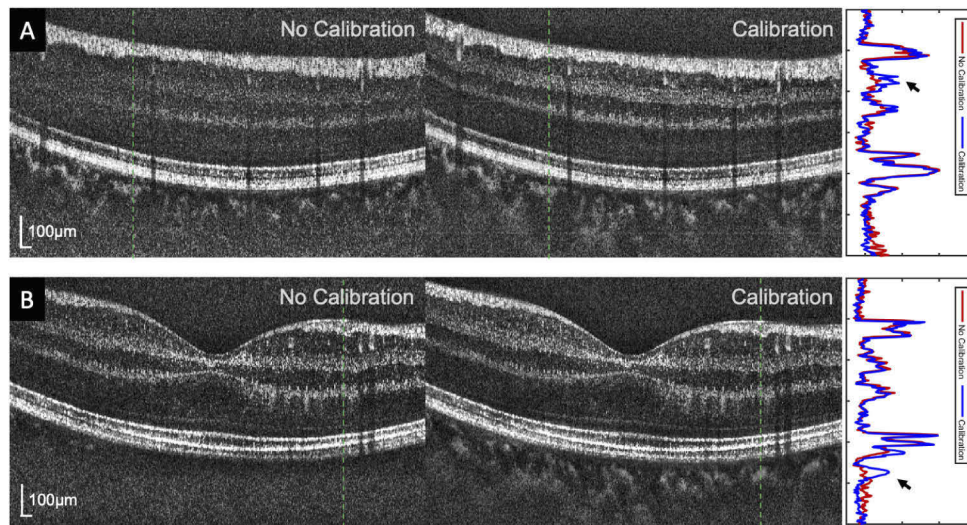


Fig. 8. In vivo retinal image using dual-balance mode acquired at two different locations showing the fringe washout in the inner retina (A) and the choroid (B). The representative A-scan intensity profile in each B-scan locations, indicated by the green dotted line, shows the depth position of the noticeable signal washout pointed by the black arrow.

Figure 9 compares the *in vivo* retinal OCTA images processed with and without the application of numerical calibration with the balanced detection mode. OCTA images were acquired using 4 repeated B-scan protocol (BM), where 4 repeated B-scans were acquired at the same location and the complex differential variance among the B-scans were calculated as blood flow contrast [27]. Here, Fig. 9(A,B) demonstrate the *en face* OCTA projection of the combination of superficial layer (e.g., superficial and intermediate vascular plexus), and (C,D) demonstrate *en face* OCTA intensity projection of deep layer (e.g., deep vascular plexus) in the inner retina. OCTA images after the numerical spectral calibration clearly shows the improved visibility of the blood vessels along with better contrast compared to the ones without calibration. However, the visibility in the vascular structure in the OCTA without numerical calibration is also depth dependent as in the case of OCT intensity B-scans shown in the previous paragraph. The green dotted box area in both the superficial and deep layer shows more prominent attenuation in the vascular signals without calibration compared to the area indicated by the orange dotted box. This is because of the depth independency in the signal attenuation as demonstrated with the mirror intensity results in the Fig. 4(D), where the signal in the inner retina is severely weakened in green dotted box.

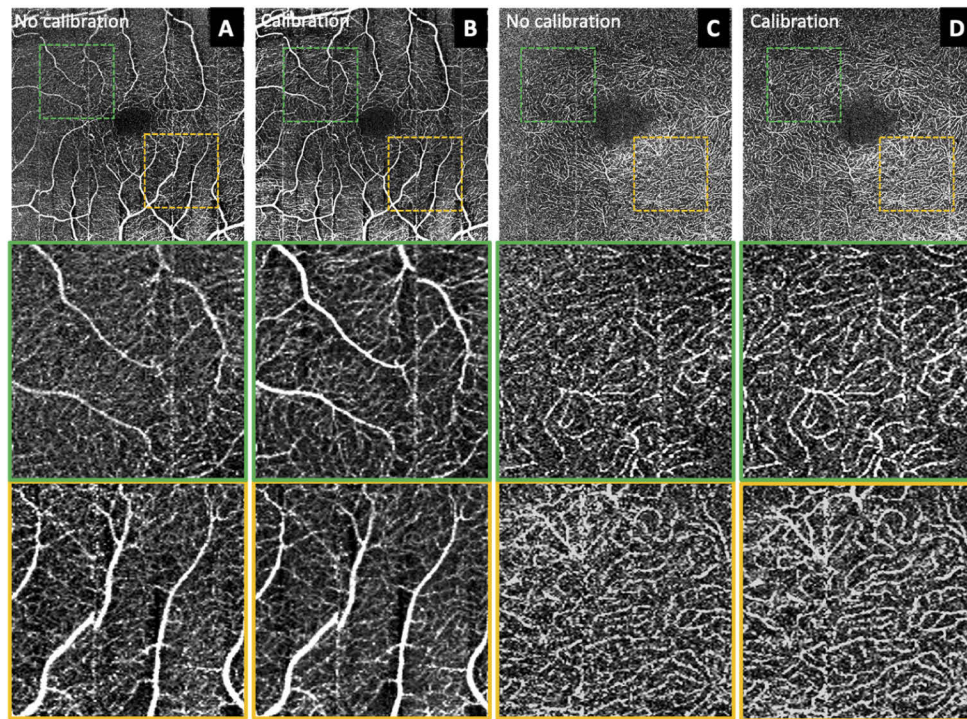


Fig. 9. *In vivo* retinal OCTA image using dual-balance mode. Superficial vascular plexus without calibration (A) shows reduced OCTA contrast due to the spectral mismatch compared to the image after calibration (B). The zoom-in OCTA images from two locations (green and orange dotted box) showing more prominent signal reduction in the area indicated by the green dotted box, corresponding to the location of signal washout in the inner retina. Deep vascular plexus without (C) and with (D) the numerical spectral calibration. The scan area is 4×4 mm.

4. Discussion

Multiple spectrometer-based configuration extends the imaging capability of the traditional SD-OCT system. Depending on the arrangement of the spectrometers and signal processing regime, previous studies have shown that improvement in the imaging speed [7,8,28,29], sensitivity [9–12], resolution [30], or imaging range [31,32] can be accomplished by implementing multiple spectrometers. In this study, two imaging modes are implemented using our dual spectrometer SD-OCT system, *e.g.*, dual-balanced detection mode and high-speed mode, to show that different clinically useful information can be obtained from these modes. This section discusses examples of different imaging applications that can be achieved from the two imaging modes by increasing the imaging speed or sensitivity of the imaging system.

Improvement in the acquisition speed allows using SD-OCT for new applications that have previously predominantly been implemented using SS-OCT. While the high-speed wide-field SS-OCT imaging leveraged the recent advancements in high-speed swept source lasers, *e.g.*, vertical cavity surface-emitting laser (VCSEL) and Fourier-domain mode-lock laser (FDML), with more than 400 kHz A-scan rate [33–35], only a few SD-OCT studies show the implementation of high-speed line-scan camera with more than 300 kHz A-scan rate [6,36]. High imaging speed is critical for acquiring motion-free photoreceptor images in adaptive optics OCT [8,37]. In addition, taking advantage of the inherent phase stability, high-speed SD-OCT system is especially

preferable for observing fast dynamic events such as quantitative blood flow measurement through Doppler imaging [38], dynamic OCT [39], optoretinograms [40,41], and mechanical wave visualization for elastography [42,43]. With the advancement of GPU processing, high-speed SD-OCT system can take advantage of real-time processing and analysis [44]. Finally, with high A-scan rate, OCTA based relative blood flow visualization can be performed [45,46].

4.1. Relative flow speed visualization using the VISTA algorithm

The visualization of relative retinal flow using the variable interscan time analysis (VISTA) algorithm can be accomplished with the 500 kHz high-speed imaging mode [45,46]. The fast A-line rate of the dual spectrometer SD-OCT configuration allows the flow dynamics to be distinguished by comparing the BM set with different intervals. In this study, we acquired images using a 6BM protocol and 500 B-scan locations, with each frame consisting of 500 A-lines sampling points. The volume acquisition time was 4.2 seconds, including time for mirror 'fly-back'. For the VISTA processing, 1.4 ms time interval OCTA images were reconstructed using the complex subtraction of adjacent BM sets (*e.g.*, 1-2, 2-3, 3-4, 4-5, 5-6) and 2.8 ms time interval OCTA images were reconstructed using every other BM set (*e.g.*, 1-3, 2-4, 3-5, 4-6). In addition, the OCTA volume calculated from all the time intervals was reconstructed by applying complex variance on the full 6BM dataset. The resulting OCTA volumes were then segmented using graph-cut to produce 2D *en face* OCTA images from the inner retina. Figure 10(A-B) shows the OCTA intensity projection from short (1.4 ms) and long-time intervals (2.8 ms). As expected, the 2.8 ms time interval produced OCTA images with more vascular features compared to the shorter time interval. The vascular mask was created from an OCTA projection image of all time-interval using a deep-learning based vessel segmentation algorithm [47], where the signal and noise can be separated as shown in Fig. 10(C). Finally, the relative vascular flow map was reconstructed by taking the intensity ratio of the short and long-time interval OCTA images at each pixel and after noise filtering using the vascular map, as presented in Fig. 10(D). Large vessels with fast flow are visualized as red and small capillary vessels with slow flow are visualized as blue. Due to the relatively long volume acquisition time of the VISTA protocol, artifacts from subject's involuntary eye motion can still appear in the OCTA images as vertical lines. Those motion artifacts can be potentially removed using multi-volume registration methods [48,49].

4.2. High-contrast visualization of microcapillaries and interconnecting vessels

The high sensitivity achieved using dual balanced detection provided better visualization of blood vessels. This is useful in quantification of microvascular networks and visualization of interconnecting vessels, typically requiring both high resolution and contrast [50,51]. Dual balanced detection mode of SD-OCT system can acquire three-dimensional microvascular structure at high spatial resolution and contrast, leading to clear visualization of capillaries and interconnecting vessels. Figure 11(A-C) shows superficial vessels, deep vessels, and interconnecting vessels acquired using DBD mode. The OCTA is acquired using 3BM protocol with each B-scan consists of 500 A-lines and at 250 kHz A-line rates. Compared to the high-speed mode, the OCTA volume acquired through DBD provides higher contrast vasculature images. The composite image of different vascular layers shows the location of interconnecting vessels, where the superficial vessels are presented in red, and interconnecting vessels are presented in yellow, and deep vessel are presented in blue (Fig. 11(D)). The OCT and OCTA B-scan images corresponding to the green and orange location in the composite image are shown in Fig. 11(E) and (F).

One current limitation of implementing multiple spectrometer-based SD-OCT system is the additional cost. Depending on the specifications of the spectrometer and the means of implementation (*e.g.*, commercial, or customized), installing an additional spectrometer can be

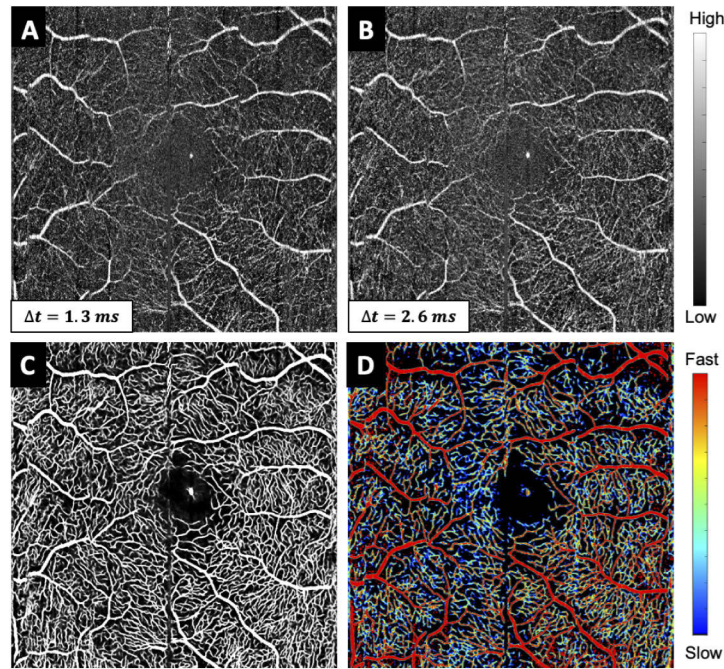


Fig. 10. Semi-quantitative visualization of flow dynamics using the VISTA processing algorithm. OCTA projection images constructed from short time interval using adjacent BM frames (A) and long time interval using every other BM frame (B). Binary vascular mask created from deep learning segmentation of combined OCTA of two interval settings (C), and relative flow velocity map (D).

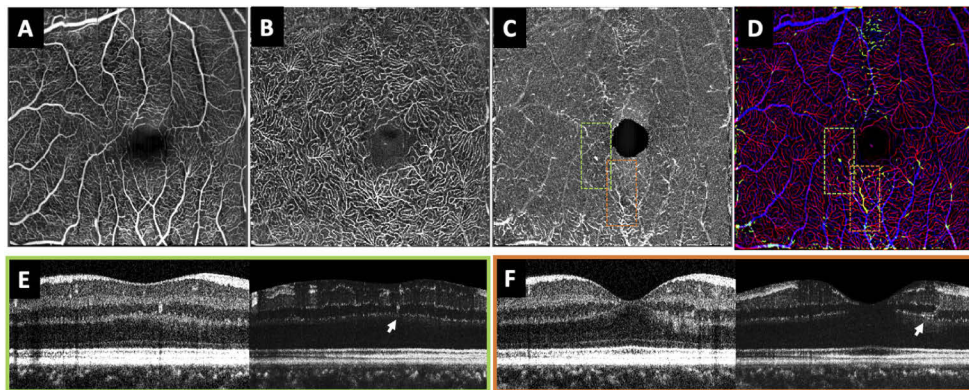


Fig. 11. High-contrast microvasculature visualization realized by dual-balanced mode. Intensity projection of superficial vessel (A), deep vessel (B), interconnecting vessels (C), and composite image of three layers (D). Representative B-scan OCT image and the OCTA B-scan images are acquired from the location with interconnecting vessels (E, F) as indicated by the orange and green dotted boxes in (C) and (D). The white arrows in the B-scan indicate the interconnecting vessels.

expensive. While a customized low-cost optical spectrometer can be designed with the help of 3D printing [52], managing system stability to prevent misalignment is the main challenge. On the other hand, commercial spectrometers are generally pre-calibrated and mechanically stable.

However, slight differences in the alignment between different spectrometer units can still be present as most of the existing SD-OCT systems are based on a single spectrometer. In addition, commercial spectrometers generally lack the freedom of alignment and are thus harder to re-align. Overall, the current high cost of implementing a multiple spectrometer-based OCT system is due to the combination of additional equipment as well as the labor cost for precise alignment and re-alignment of multiple spectrometers. The demonstrated numerical spectrometer calibration can substantially reduce the labor cost of mechanically aligning the multiple spectrometers as it can not only guide the alignment process by estimating the translation and tilt amount but also computationally align the spectrometer signals with sub-pixel precision.

5. Conclusion

Calibration of spectrometers for multiple spectrometer OCT configuration remains a critical step for acquiring images with exceptional quality, and yet is very hard to achieve solely with hardware-based alignment. In order to successfully align the spectrometers, we introduced and validated a novel numerical calibration method that effectively compensated the spectral misalignment between the spectrometers. Significant improvements in SNR and vasculature visibilities after the numerical calibration were demonstrated with a healthy human subject. The numerically calibrated dual-spectrometer SD-OCT system was demonstrated to be capable of acquiring images at high-speed mode or dual-balanced detection mode, utilities of which in clinical application are expected to have potential for providing retinal images with reduced motion artifacts or improved visibilities of micro-scale morphological features.

Funding. Canadian Cancer Society; The Paul and Edwina Heller Memorial Fund; Alzheimer Society Research Program; Canadian Institutes of Health Research; Natural Sciences and Engineering Research Council of Canada; National Institutes of Health (R01 EY031331).

Disclosures. MVS: Seymour Vision (I).

Data Availability. Data underlying the results presented in this paper are not publicly available at this time but may be obtained from the authors upon reasonable request.

References

1. B. E. Bouma, S. H. Yun, B. J. Vakoc, M. J. Suter, and G. J. Tearney, "Fourier-domain optical coherence tomography: recent advances toward clinical utility," *Curr. Opin. Biotechnol.* **20**(1), 111–118 (2009).
2. Z. Yaqoob, J. Wu, and C. Yang, "Spectral domain optical coherence tomography: a better oct imaging strategy," *BioTechniques* **39**(6S), S6–S13 (2005).
3. A. C. Sull, L. N. Vuong, L. L. Price, V. J. Srinivasan, I. Gorczynska, J. G. Fujimoto, J. S. Schuman, and J. S. Duker, "Comparison of spectral/fourier domain optical coherence tomography instruments for assessment of normal macular thickness," *Retina* **30**(2), 235–245 (2010).
4. J. F. Boer, *Spectral/Fourier Domain Optical Coherence Tomography* (Springer, 2015).
5. A. R. Miller, L. Roisman, Q. Zhang, F. Zheng, J. R. de Oliveira Dias, Z. Yehoshua, K. B. Schaal, W. Feuer, G. Gregori, Z. Chu, C. L. Chen, S. Kubach, L. An, P. F. Stetson, M. K. Durbin, R. K. Wang, and P. J. Rosenfeld, "Comparison between spectral-domain and swept-source optical coherence tomography angiographic imaging of choroidal neovascularization," *Invest. Ophthalmol. Visual Sci.* **58**(3), 1499–1505 (2017).
6. M. Münter, M. Pieper, T. Kohlfaerber, E. Bodenstorfer, M. Ahrens, C. Winter, R. Huber, P. König, G. Hüttmann, and H. Schulz-Hildebrandt, "Microscopic optical coherence tomography (moct) at 600 khz for 4d volumetric imaging and dynamic contrast," *Biomed. Opt. Express* **12**(10), 6024–6039 (2021).
7. L. An, P. Li, R. Wang, and T. T. Shen, "High speed spectral domain optical coherence tomography for retinal imaging at 500,000 a-lines per second," *Biomed. Opt. Express* **2**(10), 2770–2783 (2011).
8. O. P. Kocaoglu, T. L. Turner, Z. Liu, and D. T. Miller, "Adaptive optics optical coherence tomography at 1 mhz," *Biomed. Opt. Express* **5**(12), 4186 (2014).
9. A. Bradu and A. G. Podoleanu, "Fourier domain optical coherence tomography system with balance detection," *Opt. Express* **20**(16), 17522–17538 (2012).
10. W.-C. Kuo, C.-M. Lai, Y.-S. Huang, C.-Y. Chang, and Y.-M. Kuo, "Balanced detection for spectral domain optical coherence tomography," *Opt. Express* **21**(16), 19280 (2013).
11. A. M. Kho and V. J. Srinivasan, "Proactive spectrometer matching for excess noise suppression in balanced visible light optical coherence tomography (oct)," *Opt. Express* **29**(25), 42037–42054 (2021).
12. E. Bo, X. Liu, and L. Liu, "Signal-to-noise ratio enhanced spectral domain optical coherence tomography with dual-balanced detection," *Procedia Eng.* **140**, 140–143 (2016).

13. Q. Xiong, N. Wang, X. Liu, S. Chen, H. Liang, S. Chen, and L. Liu, "Single input state polarization-sensitive optical coherence tomography with high resolution and polarization distortion correction," *Opt. Express* **27**(5), 6910 (2019).
14. D. Yang, M. Zhang, M. Hu, and Y. Liang, "High-resolution polarization-sensitive optical coherence tomography for zebrafish muscle imaging," *Biomed. Opt. Express* **11**(10), 5618–5632 (2020).
15. M. Szkulmowski, S. Tamborski, and M. Wojtkowski, "Spectrometer calibration for spectroscopic fourier domain optical coherence tomography," *Biomed. Opt. Express* **7**(12), 5042 (2016).
16. Y. C. Sun, C. Huang, G. Xia, S. Q. Jin, and H. B. Lu, "Accurate wavelength calibration method for compact ccd spectrometer," *J. Opt. Soc. Am. A* **34**(4), 498–505 (2017).
17. C. C. Rosa and A. G. Podoleanu, "Limitation of the achievable signal-to-noise ratio in optical coherence tomography due to mismatch of the balanced receiver," *Appl. Opt.* **43**(25), 4802–4815 (2004).
18. Y. Chen, D. M. de Bruin, C. Kerbage, J. F. de Boer, D. Huang, E. A. Swanson, C. P. Lin, J. S. Schuman, W. G. Stinson, W. Chang, M. R. Hee, T. Flotte, K. Gregory, C. A. Puliafito, and J. G. Fujimoto, "Spectrally balanced detection for optical frequency domain imaging," *Opt. Express* **15**(25), 16390–16399 (2007).
19. Y. Miao, J. Song, M. Siadati, D. Ma, Y. Jian, M. F. Beg, M. V. Sarunic, and M. J. Ju, "Phase-corrected buffer averaging for enhanced oct angiography using fdml laser," *Opt. Lett.* **46**(16), 3833–3836 (2021).
20. A. M. Kho, T. Zhang, J. Zhu, C. W. Merkle, and V. J. Srinivasan, "Incoherent excess noise spectrally encodes broadband light sources," *Light: Sci. Appl.* **9**(1), 172 (2020).
21. M. J. Ju, M. Heisler, A. Athwal, M. V. Sarunic, and Y. Jian, "Effective bidirectional scanning pattern for optical coherence tomography angiography," *Biomed. Opt. Express* **9**(5), 2336–2350 (2018).
22. I. Rubino, D. A. Miller, R. Kuranov, Y. Wang, R. Fang, N. J. Volpe, and H. F. Zhang, "High-speed balanced-detection visible-light optical coherence tomography in the human retina using subpixel spectrometer calibration," *IEEE Transactions on Medical Imaging* (2022).
23. D. W. Ball, *Field Guide to Spectroscopy* (SPIE, 2006).
24. S. J. Wright, "Coordinate descent algorithms," *Math. Program* **151**(1), 3–34 (2015).
25. R. L. Burden and J. D. Faires, *The Bisection Algorithm* (PWS Publishers, 1985), 3rd ed.
26. Y. Yasuno, V. D. Madjarova, S. Makita, M. Akiba, A. Morosawa, C. Chong, T. Sakai, K.-P. Chan, M. Itoh, T. Yatagai, A. F. Fercher, C. K. Hitzinger, G. Kamp, S. Y. El-Zaiat, D. Huang, E. A. Swanson, C. P. Lin, J. S. Schuman, W. G. Stinson, W. Chang, M. R. Hee, T. Flotte, K. Gregory, C. A. Puliafito, J. G. Fujimoto, W. Drexler, U. Morgner, F. X. Kartner, C. Pitris, S. A. Boppart, X. D. Li, E. P. Ippen, B. Povazay, K. Bizheva, A. Unterhuber, B. Hermann, H. Sattmann, A. Apolonski, W. J. Wadsworth, J. C. Knight, P. J. S. Russell, and M. Vetterlein, "Three-dimensional and high-speed swept-source optical coherence tomography for in vivo investigation of human anterior eye segments," *Opt. Express* **13**, 1221–1223 (1991).
27. A. S. Nam, I. Chico-Calero, B. J. Vakoc, A. Mariampillai, B. A. Standish, E. H. Moriyama, M. Khurana, N. R. Munce, M. K. K. Leung, J. Jiang, A. E. Cable, B. C. Wilson, I. A. Vitkin, V. X. D. Yang, B. J. Vakoc, R. M. Lanning, J. A. Tyrell, T. P. Padera, L. A. Bartlett, T. Stylianopoulos, L. L. Munn, G. J. Tearney, D. Fukumura, R. K. Jain, and B. E. Bouma, "Complex differential variance algorithm for optical coherence tomography angiography," *Biomed. Opt. Express* **5**(11), 3822–3832 (2014).
28. L. An, G. Guan, and R. K. Wang, "High-speed 1310 nm-band spectral domain optical coherence tomography at 184,000 lines per second," *J. Biomed. Opt.* **16**(6), 060506 (2011).
29. D. Seong, D. Jeon, R. E. Wijesinghe, K. Park, H. Kim, E. Lee, M. Jeon, and J. Kim, "Ultrahigh-speed spectral-domain optical coherence tomography up to 1-mhz a-scan rate using space-time-division multiplexing," *IEEE Trans. Instrum. Meas.* **70**, 1–8 (2021).
30. D. Cui, J. Zhang, J. Gu, L. Liu, P. Shum, S. Ding, X. Yu, X. Liu, and Y. Luo, "Dual spectrometer system with spectral compounding for 1-um optical coherence tomography in vivo," *Opt. Lett.* **39**(23), 6727–6730 (2014).
31. L. Wang and L. Liu, "Corneal imaging with extended imaging range using dual spectrometer high-resolution SD-OCT," *Conference on Lasers and Electro-Optics (2019)*, paper JTu2A.6 (2019).
32. M. V. Sarunic, B. E. Applegate, and J. A. Izatt, "Real-time quadrature projection complex conjugate resolved Fourier domain optical coherence tomography," *Opt. Lett.* **31**(16), 2426 (2006).
33. S. Ni, X. Wei, R. Ng, S. Ostmo, M. F. Chiang, D. Huang, Y. Jia, J. P. Campbell, and Y. Jian, "High-speed and widefield handheld swept-source oct angiography with a vcsel light source," *Biomed. Opt. Express* **12**(6), 3553 (2021).
34. J. P. Kolb, T. Klein, C. L. Kufner, W. Wieser, A. S. Neubauer, and R. Huber, "Ultra-widefield retinal mhz-oct imaging with up to 100 degrees viewing angle," *Biomed. Opt. Express* **6**(5), 1534–1552 (2015).
35. X. Wei, T. T. Hormel, Y. Guo, and Y. Jia, "75-degree non-mydratic single-volume optical coherence tomographic angiography," *Biomed. Opt. Express* **10**(12), 6286–6295 (2019).
36. B. Potsaid, I. Gorczynska, V. J. Srinivasan, Y. Chen, J. Jiang, A. Cable, and J. G. Fujimoto, "Ultrahigh speed spectral/Fourier domain OCT ophthalmic imaging at 70,000 to 312,500 axial scans per second," *Opt. Express* **16**(19), 15149 (2008).
37. M. Azimpour, R. J. Zawadzki, I. Gorczynska, J. Migacz, J. S. Werner, and R. S. Jonnal, "Intraframe motion correction for raster-scanned adaptive optics images using strip-based cross-correlation lag biases," *PLoS One* **13**(10), e0206052 (2018).
38. Y.-C. Ahn, W. Jung, and Z. Chen, "Quantification of a three-dimensional velocity vector using spectral-domain doppler optical coherence tomography," *Opt. Lett.* **32**(11), 1587–1589 (2007).

39. I. A. El-Sadek, A. Miyazawa, L. T.-W. Shen, S. Makita, S. Fukuda, T. Yamashita, Y. Oka, P. Mukherjee, S. Matsusaka, T. Oshika, H. Kano, and Y. Yasuno, "Optical coherence tomography-based tissue dynamics imaging for longitudinal and drug response evaluation of tumor spheroids," *Biomed. Opt. Express* **11**(11), 6231–6248 (2020).
40. V. P. Pandiyan, A. Maloney-Bertelli, J. A. Kuchenbecker, K. C. Boyle, T. Ling, Z. C. Chen, B. H. Park, A. Roorda, D. Palanker, and R. Sabesan, "The optoretinogram reveals the primary steps of phototransduction in the living human eye," *Sci. Adv.* **6**(37), 1 (2020).
41. M. Azimipour, D. Valente, K. V. Vienola, J. S. Werner, R. J. Zawadzki, and R. S. Jonnal, "Optoretinogram: optical measurement of human cone and rod photoreceptor responses to light," *Opt. Lett.* **45**(17), 4658–4661 (2020).
42. C.-H. Liu, A. Schill, C. Wu, M. Singh, and K. V. Larin, "Non-contact single shot elastography using line field low coherence holography," *Biomed. Opt. Express* **7**(8), 3021 (2016).
43. Y. Li, S. Moon, J. J. Chen, Z. Zhu, and Z. Chen, "Ultrahigh-sensitive optical coherence elastography," *Light: Sci. Appl.* **9**(1), 58 (2020).
44. S. Borkovkina, A. Camino, W. Janponsri, M. V. Sarunic, and Y. Jian, "Real-time retinal layer segmentation of OCT volumes with GPU accelerated inferencing using a compressed, low-latency neural network," *Biomed. Opt. Express* **11**(7), 3968–3984 (2020).
45. T.-H. Chen, Y.-C. Wu, T.-Y. Tsai, C.-B. Chueh, B.-H. Huang, Y.-P. Huang, M.-T. Tsai, Y. Yasuno, and H.-C. Lee, "Effect of a-scan rate and interscan interval on optical coherence angiography," *Biomed. Opt. Express* **12**(2), 722–736 (2021).
46. S. B. Ploner, E. M. Moul, W. Choi, N. K. Waheed, B. Lee, E. A. Novais, E. D. Cole, B. Potsaid, L. Husvagt, J. Schottenhamml, A. Maier, P. J. Rosenfeld, J. S. Duker, J. Hornegger, and J. G. Fujimoto, "Toward quantitative optical coherence tomography angiography: visualizing blood flow speeds in ocular: Pathology using variable interscan time analysis," *Retina* **36**(Supplement 1), S118–S126 (2016).
47. J. Lo, M. Heisler, V. Vanzan, S. Karst, I. Z. Matovinovic, S. Loncaric, E. V. Navajas, M. F. Beg, and M. V. Šarunic, "Microvasculature segmentation and intercapillary area quantification of the deep vascular complex using transfer learning," *Trans. Vis. Sci. Tech.* **9**(2), 38 (2020).
48. A. Athwal, C. Balaratnasingam, D.-Y. Yu, M. Heisler, M. V. Sarunic, and M. J. Ju, "Optimizing 3D retinal vasculature imaging in diabetic retinopathy using registration and averaging of oct-a," *Biomed. Opt. Express* **12**(1), 553 (2021).
49. Y. Cheng, Z. Chu, and R. K. Wang, "Robust three-dimensional registration on optical coherence tomography angiography for speckle reduction and visualization," *Quant. Imaging Med. Surg.* **11**(3), 879–894 (2020).
50. J. Zhu, M. T. Bernucci, C. W. Merkle, and V. J. Srinivasan, "Visibility of microvessels in optical coherence tomography angiography depends on angular orientation," *J. Biophotonics* **13**(10), e202000090 (2020).
51. J. P. Campbell, M. Zhang, T. S. Hwang, S. T. Bailey, D. J. Wilson, Y. Jia, and D. Huang, "Detailed vascular anatomy of the human retina by projection-resolved optical coherence tomography angiography," *Sci. Rep.* **7**(1), 42201 (2017).
52. S. Kim, M. Crose, W. J. Eldridge, B. Cox, W. J. Brown, A. Wax, D. Huang, E. A. Swanson, C. P. Lin, J. S. Schuman, W. G. Stinson, W. Chang, M. R. Hee, T. Flotte, K. Gregory, C. A. Puliafito, W. Jung, S. I. Sayegh, D. T. McCormick, J. Kim, S. A. Boppart, Y. S. Zhang, J. B. Chang, M. M. Alvarez, G. T. de Santiago, J. Aleman, B. Batzaya, V. Krishnadoss, A. A. Ramanujam, M. Kazemzadeh-Narbat, F. Chen, P. W. Tillberg, M. R. Dokmeci, E. S. Boyden, A. Khademhosseini, S. Knowlton, A. Joshi, P. Syrrist, A. F. Coskun, S. Tasoglu, C. D. Lu, M. F. Kraus, B. Potsaid, J. J. Liu, W. Choi, V. Jayaraman, A. E. Cable, J. Hornegger, J. S. Duker, J. G. Fujimoto, M. Jeon, E. J. Chaney, C. N. Stewart, H. C. Lee, D. Vermeulen, L. Chen, T. Nielsen, S. Y. Park, A. Ghaemi, E. Swanson, and C. Doerr, "Design and implementation of a low-cost, portable OCT system," *Biomed. Opt. Express* **9**(3), 1232–1243 (2018).